Electronic Supplementary Material (ESI) for Nanoscale.
This journal is © The Royal Society of Chemistry 2018

Supplementary Information

Nanoscale chemical imaging of solid-liquid interfaces using tip-enhanced Raman spectroscopy

Naresh Kumar,[a,b] Weitao Su[c], Martin Veselý[b], Bert M. Weckhuysen[b], Andrew J. Pollard[a] and Andrew J. Wain[a]

---

[a] *National Physical Laboratory, Teddington, Middlesex, U.K. TW11 0LW*
[b] *Faculty of Science, Debye Institute for Nanomaterials Science, Utrecht University, Universiteitsweg 99, 3584 CG Utrecht, The Netherlands.*
[c] *College of Materials and Environmental Engineering, Hangzhou Dianzi University, 310018 Hangzhou, China*

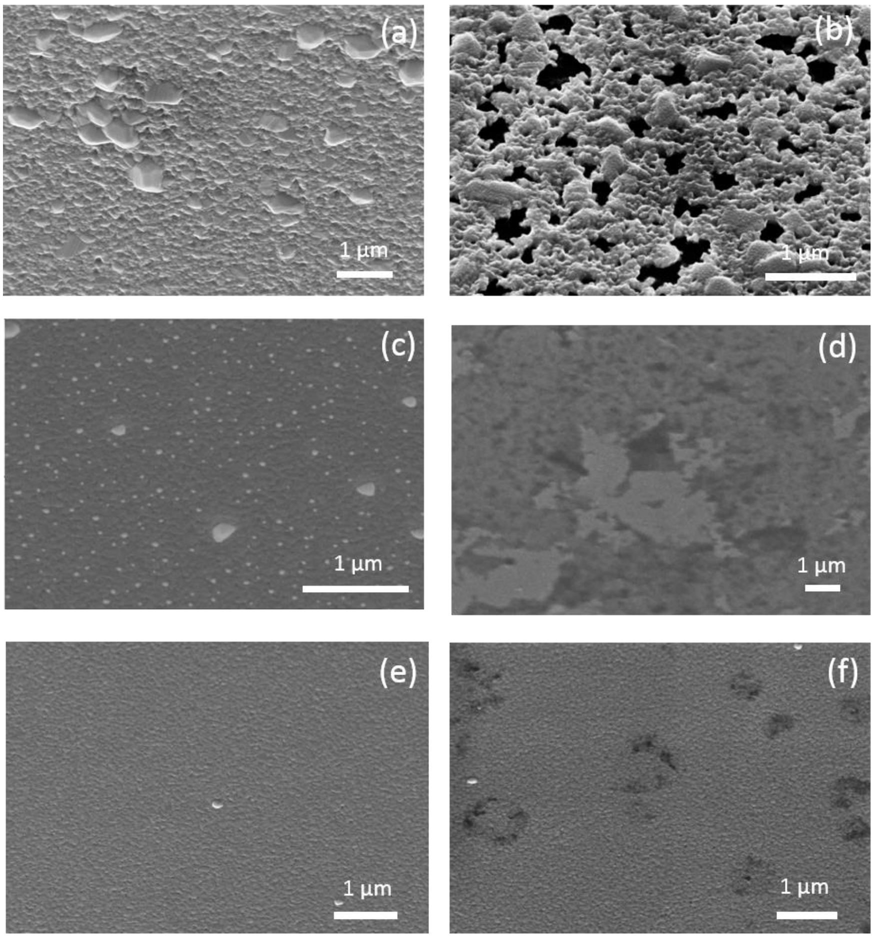

Fig. S1. Stability of TERS probes with different types of metal coating in water. (a) SEM image of cantilever of the Ag coated TERS probe shown in Fig. 2a. (b) SEM image of cantilever of the Ag coated TERS probe after immersing in water for 1 h shown in Fig. 2b. (c) SEM image of cantilever of the Cr-Ag coated TERS probe shown in Fig. 2c. (d) SEM image of cantilever of the Cr-Ag coated TERS probe after immersing in water for 1 h shown in Fig. 2d. (e) SEM image of cantilever of the Cr-Au-Ag coated TERS probe shown in Fig. 2e. (f) SEM image of cantilever of the Cr-Au-Ag coated TERS probe after immersing in water for 1 h shown in Fig. 2f. The origin of the circular patches observed in Fig. 2f is not clear, but the shape is consistent with a "coffee ring effect" resulting from residue remaining on the surface after evaporation of the water.

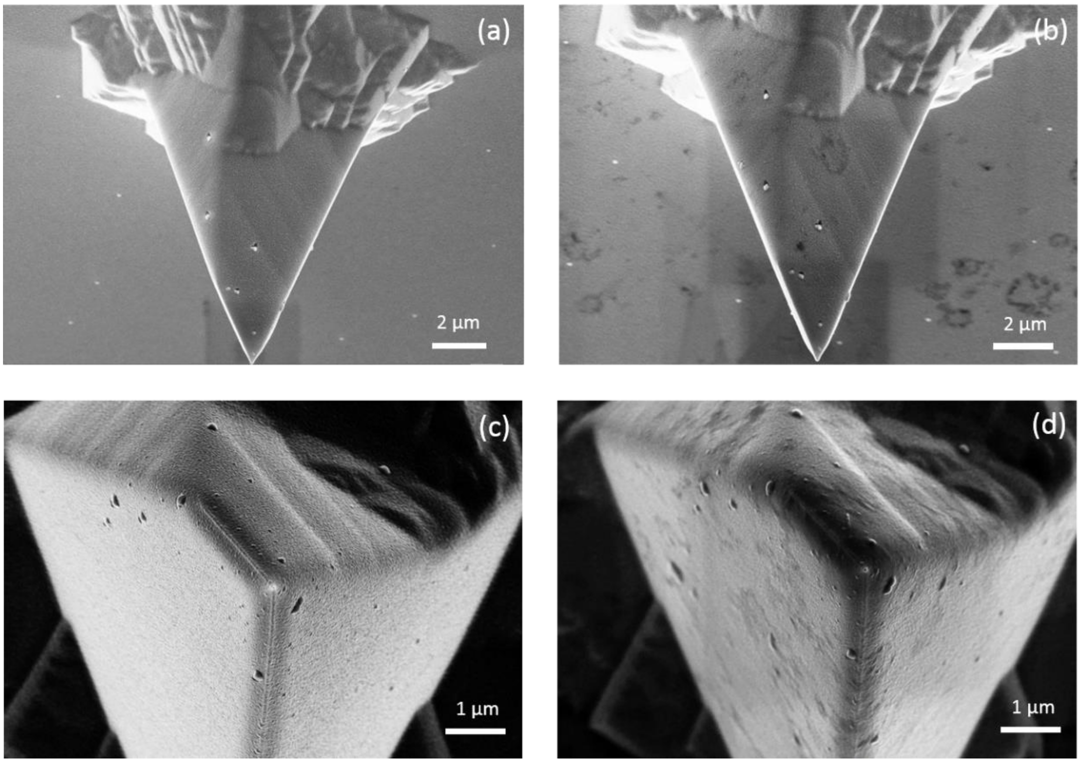

Fig. S2. Stability of Cr-Au-Ag coated TERS probes in water. (a), (c) SEM images of two Cr-Au-Ag coated TERS probes before immersion in water. (b), (d) SEM images of the TERS probes shown in (a) and (c), respectively after immersion in water for 1 h. It should be noted that the Ag coating of TERS probes is fully preserved after exposure to water. As in Fig. S1, there is evidence of the “coffee ring effect” in Fig. S2b and S2d.

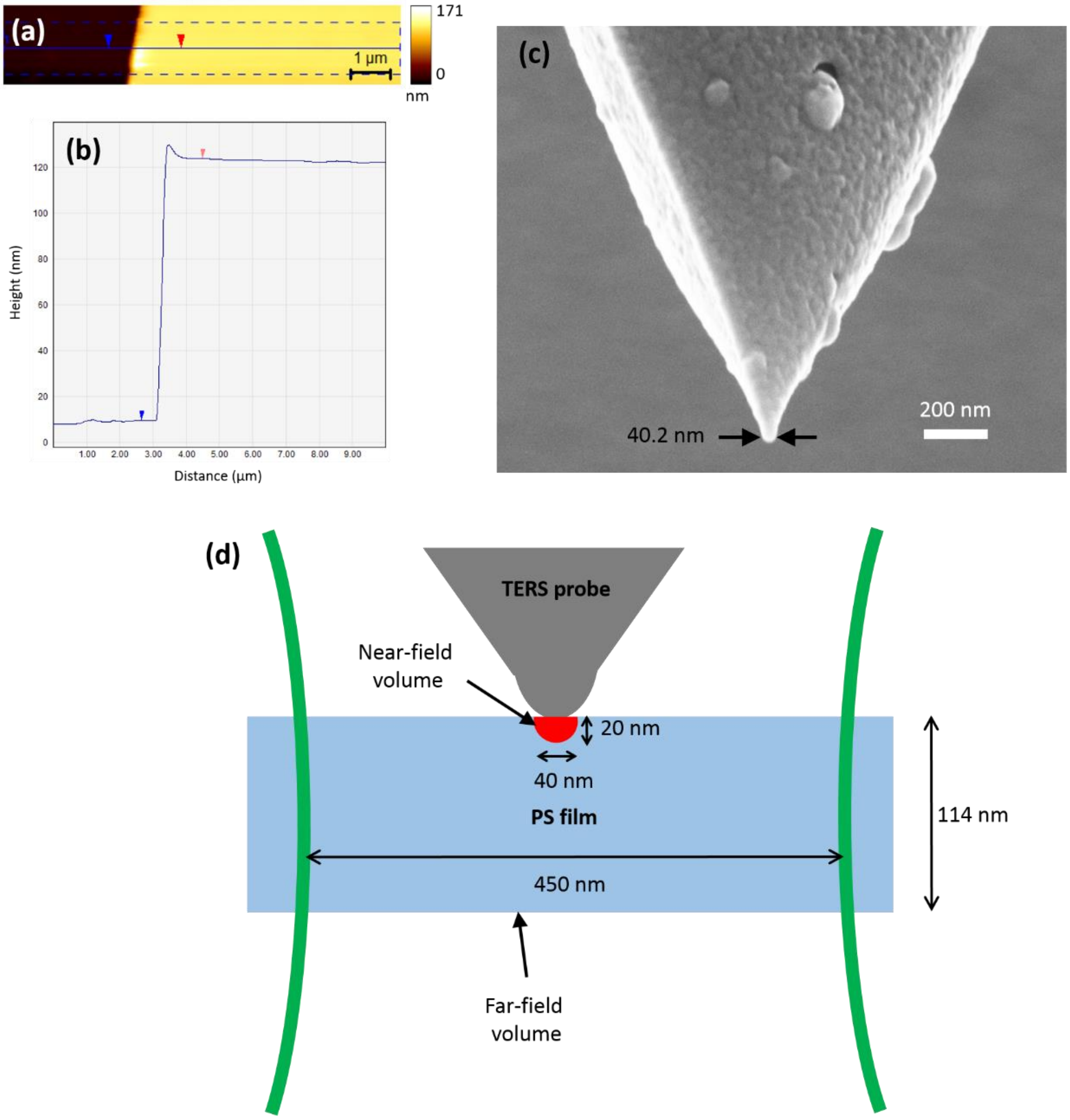

Fig. S3. (a) AFM topography image of a scratch on the PS film. (b) Average line profile across the step in (a) between the horizontal dashed lines indicated. The thickness of the PS film is estimated from the average height of this step between the blue and red markers to be 114 nm. (c) SEM image of a representative Cr-Au-Ag coated TERS probe-apex. The diameter of the probe-apex is estimated to be approximately 40 nm. (d) Schematic diagram illustrating the far-field and near-field sampling volumes, used for estimating the EF of TERS measurements on the PS sample (not to scale). For the Raman system used in this work the laser spot size is estimated to be 450 nm, based on confocal imaging of SWCNTs, and the axial resolution is of the order of 1000 nm, estimated from vertical measurements of a single-layer graphene flake. The far-field sampling volume of the system is therefore approximated to a cylinder with a diameter equal to 450 nm and a height equal to the PS film thickness (114 nm), yielding a value of 7.25×10^7 nm^3. The lateral size of the near-field enhancement is usually estimated from the size of the TERS probe-apex (J. Raman Spectrosc. 2009, 40(10), 1392; Anal. Bioanal. Chem. 2008, 391(5), 1907; Nano Lett. 2010, 10(11), 4514; Appl. Phys. Lett. 2014, 104, 123106; Nanoscale, 2015, 7, 7133–7137; Nanoscale, 2017, 9, 2723–2731). Furthermore, the Raman enhancement has been shown to decay within a distance comparable to the radius of the TERS probe-apex (J. Raman Spectrosc. 2003, 34, 663–667; Surface Science 2009, 603, 1335–1341; Phys. Rev. Lett. 2009, 103, 186101; Nanoscale, 2017, 9, 2723–2731). Therefore, the near-field sampling volume is approximated to a hemisphere underneath the TERS probe apex with a radius of 20 nm, giving a value of 1.68×10^4 nm^3.

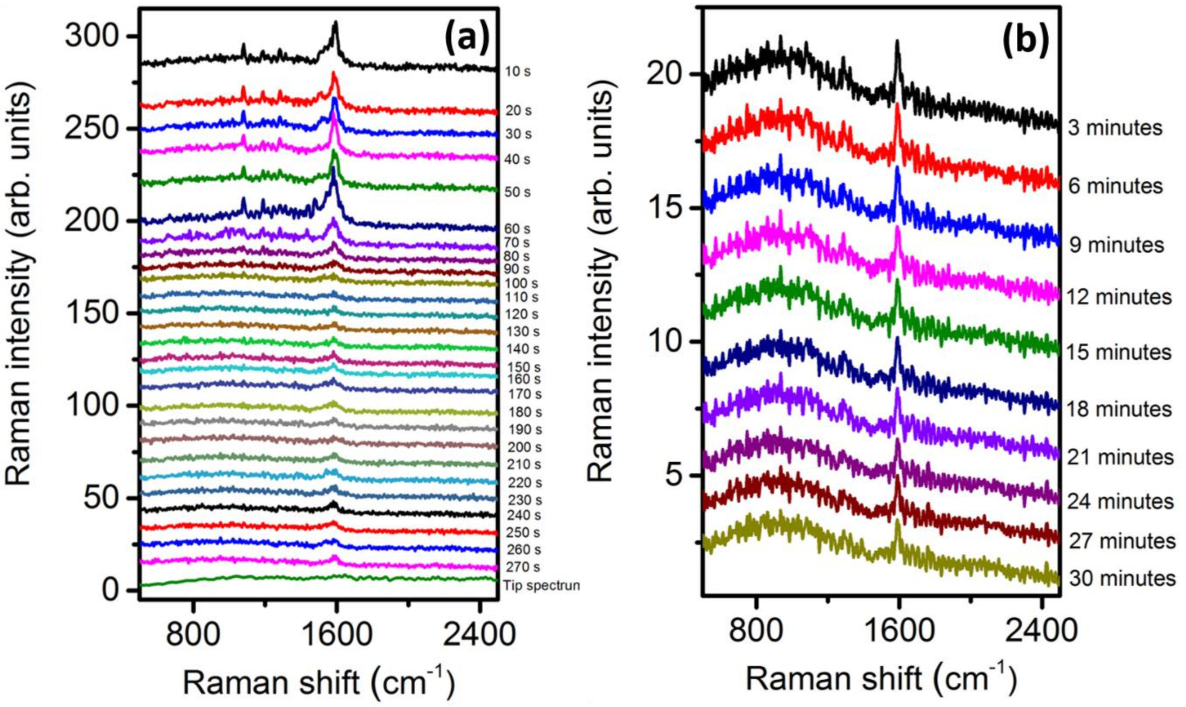

Fig. S4 (a) Time-series TERS spectra measured from BPT SAM on Au in air at intervals of 10 s. Integration time: 1 s. Plot of the 1593 cm^{-1} TERS band intensity versus time is shown in Fig. 3e. (b) Time-series TERS spectra measured from BPT SAM on Au in water at intervals of 3 minutes. Integration time: 60s. Plot of the 1593 cm^{-1} TERS intensity versus time is shown in Fig. 3f. TERS spectra measured from the BPT SAM in water have been normalised by integration time for comparison with the corresponding measurements in air. Spectra have been shifted vertically in (a) and (b) for easier visualisation. The time-series spectra presented in (a) and (b) were measured using the same TERS probe. After performing the time-series TERS measurements shown in (a) and (b) the cleanliness of the TERS probe was checked on a clean Au-coated glass coverslip. The tip spectrum plotted in Fig. S3a (last spectrum) confirms the cleanliness of the TERS probe.

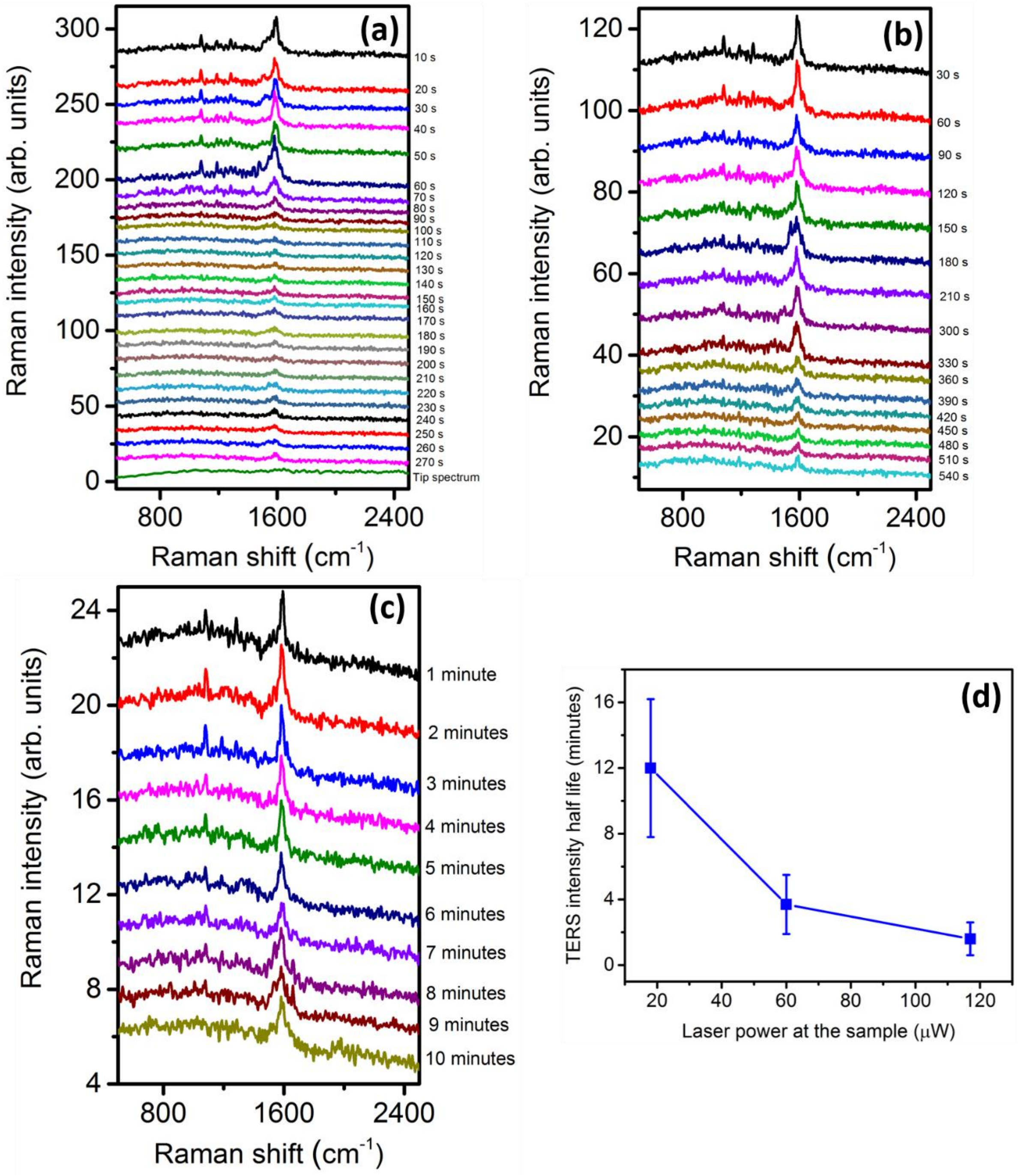

Fig. S5 (a) Time-series TERS spectra measured from BPT SAM on Au in air using (a) 117 µW (b) 60 µW (c) 18 µW laser power at the sample. Integration time: 1s. Spectra have been shifted vertically for easier visualisation. (d) Plot of the half-life of 1593 cm^{-1} TERS intensity versus laser power at the sample based on time-series TERS measurements using three nominally identical probes. Half-life is defined as the time for the TERS signal intensity to reduce to half of its initial value. The TERS intensity half-life is found to be negatively correlated with the excitation laser power at the sample consistent with laser-induced thermal desorption of the SAM under the enhanced electric field of the TERS probe. The time-series spectra presented in (a) – (c) were measured using the same TERS probe. After performing the time-series TERS measurements shown in (a) – (c) the cleanliness of the TERS probe was checked on a clean Au-coated glass coverslip. The tip spectrum plotted in Fig. S4a (last spectrum) confirms cleanliness of the TERS probe.

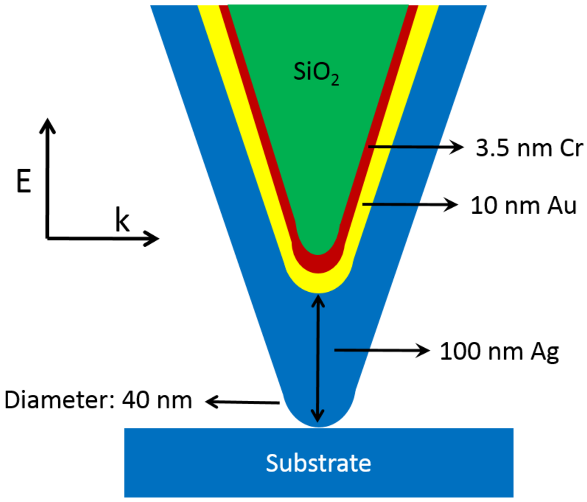

Fig. S6. Schematic diagram of the model used for numerical simulations to calculate electric field enhancement at the apex of a Cr-Au-Ag coated TERS probe. For numerical simulations, conical SiO_2/Ag probes with a spherical apex were used in the geometric model constructed in COMSOL Multiphysics®, a commercial finite element modelling software. The probe and sample characteristics were modelled on the properties of the probes used experimentally in this work. The height and cone angle of the TERS probe were set to 450 nm and 45°, respectively. The nominal thickness of Cr, Au and Ag films on SiO_2 probe were set to 3.5 nm, 10 nm and 100 nm, respectively with the apex diameter of 40 nm. For gap mode calculations, the thickness of the Au film on glass substrate was set to 10 nm. Since all experimental measurements were performed in contact-mode AFM, the distance between the Ag-coated probe and the sample was set as 0.5 nm. An extremely fine physics-controlled mesh was used with a minimum mesh size of 0.2 nm between the probe-apex and the sample surface. In order to simplify the calculations, a plane electromagnetic wave with 532 nm wavelength was incident on the TERS probe from the left side, with electric field parallel to the probe-axis. This configuration mimics the focal place of radially-polarised light (as used in this study), in which the most of the electric field in the laser spot is aligned parallel to the probe-axis.

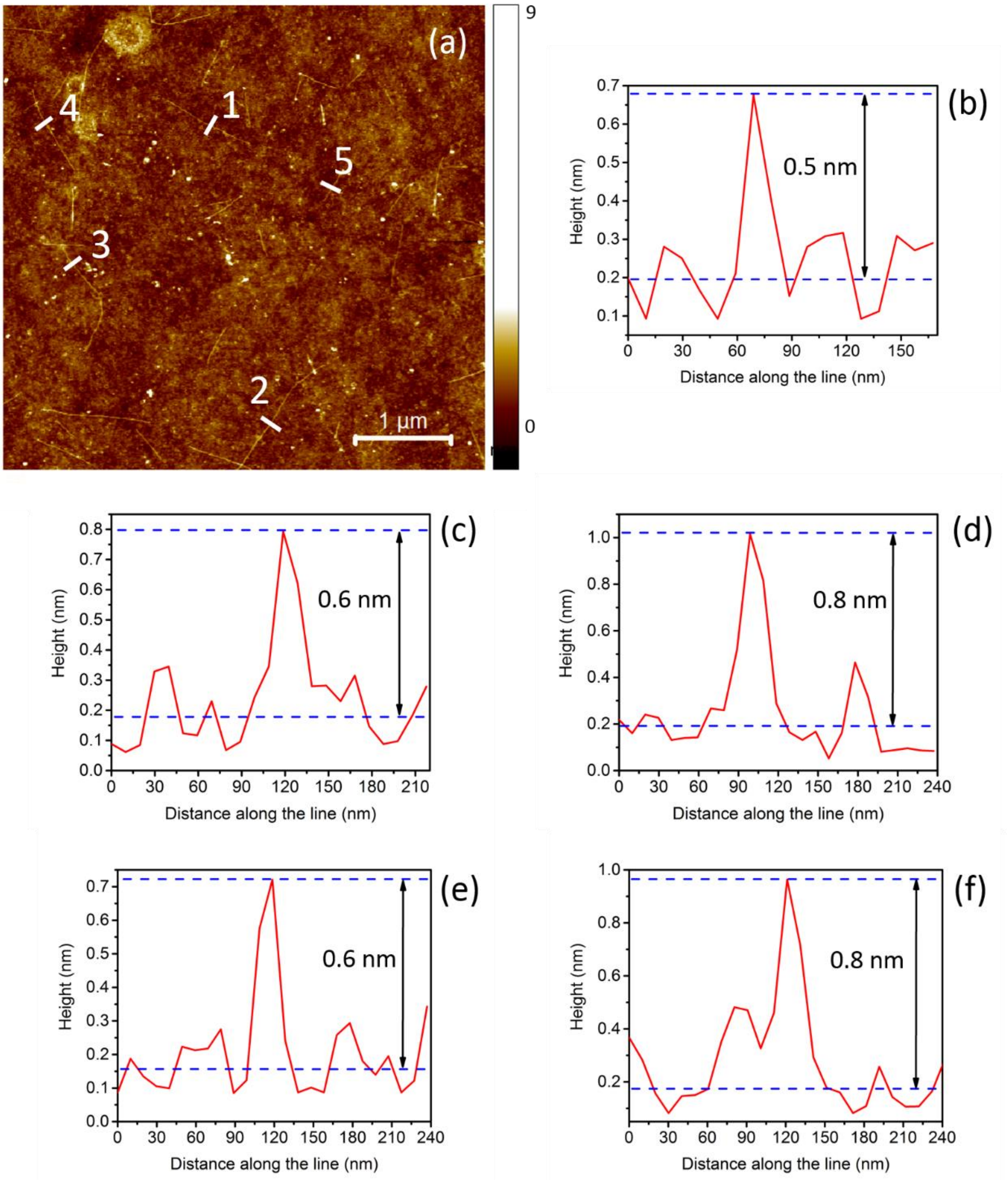

Fig. S7. (a) Larger area AFM topography image of the region shown in Fig. 5a showing the distribution of SWCNTs over a glass substrate. (b) – (f) Height profiles along the lines marked from 1 – 5 in (a). The size of the SWCNTs is estimated to be 0.7 ± 0.1 nm, indicating that the carbon nanotubes are indeed single-walled and are singly distributed over the glass substrate.

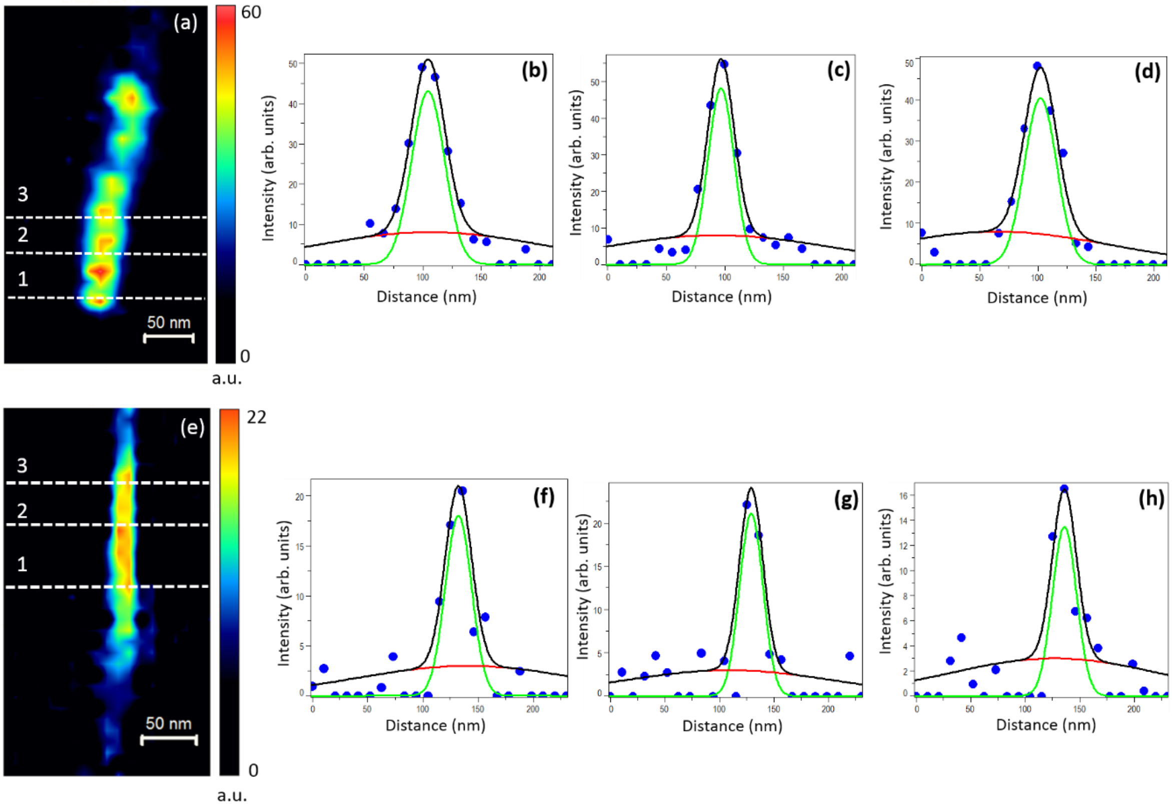

Fig. S8. (a) TERS map of the G-band intensity of a SWCNT measured in air on a glass substrate, shown in Fig. 5c of the main text. Pixel size: 10 nm. (b) – (c) Plots of line profiles marked as 1 – 3 in (a) with fitted Gaussian curves for the far-field and near-field. The average spatial resolution of the TERS map is estimated from the FWHM of the fitted Gaussian curves to be 28 ± 2 nm. (e) TERS map of the G-band intensity of a SWCNT measured in water on a glass substrate, shown in Fig. 5e of the main text. Pixel size: 10 nm. (f) – (g) Plots of line profiles marked as 1 – 3 in (e) with fitted Gaussian curves for the far-field and near-field. The average spatial resolution of the TERS map is estimated from the FWHM of the fitted Gaussian curves to be 26 ± 2 nm.

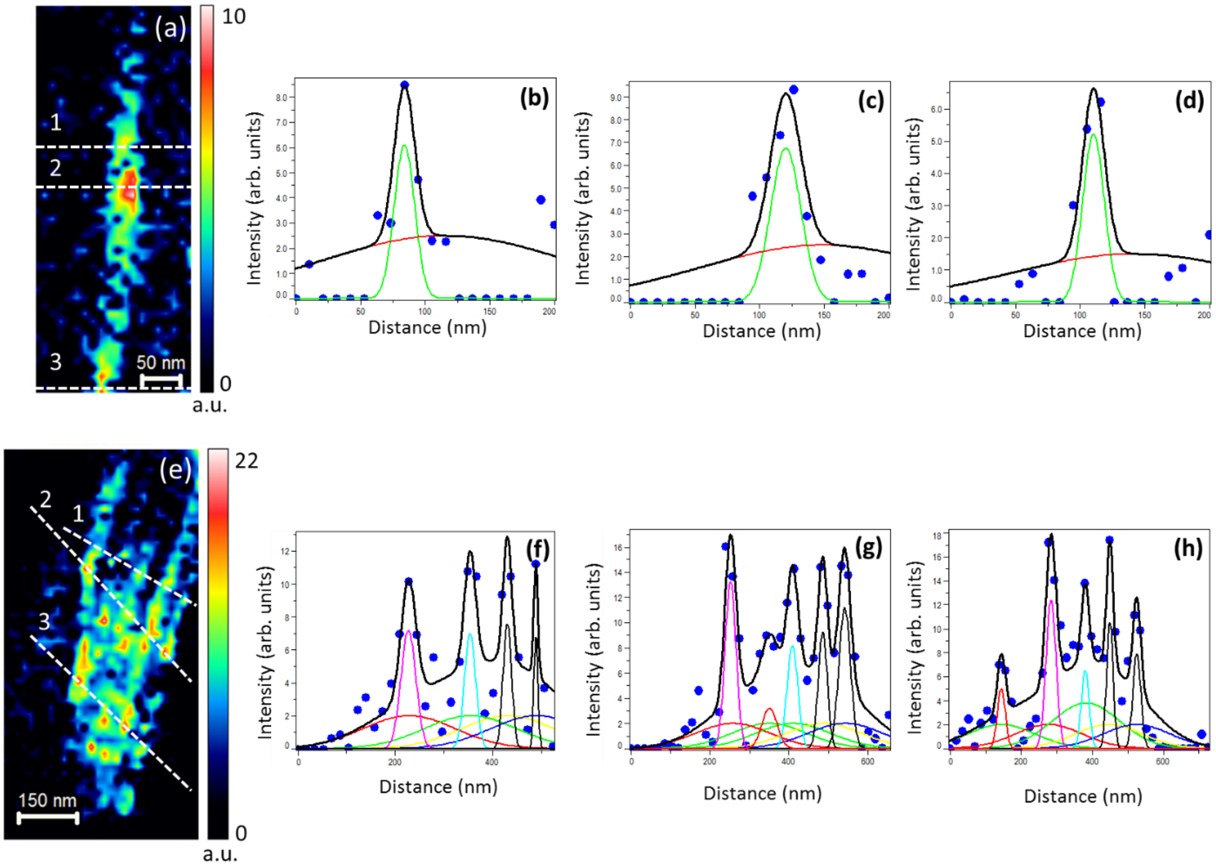

Fig. S9. Additional TERS maps of SWCNTs measured in air. (a) TERS map of the G-band intensity of a SWCNT measured in air on a glass substrate. Pixel size: 10 nm. (b) – (c) Plots of line profiles marked as 1 – 3 in (a) with fitted Gaussian curves for the far-field and near-field. The spatial resolution of the TERS map is estimated from the FWHM of the fitted Gaussian curves to be 22 ± 5 nm. (e) TERS map of the G-band intensity of a bundle of SWCNTs measured in air on a glass substrate. Pixel size: 10 nm. (f) – (g) Plots of line profiles marked as 1 – 3 in (e) with fitted Gaussian curves for the far-field and near-field. Four or five SWCNTs can be distinguished in each line profile. The spatial resolution of the TERS map is estimated from the FWHM of the fitted Gaussian curves to be 27 ± 4 nm.

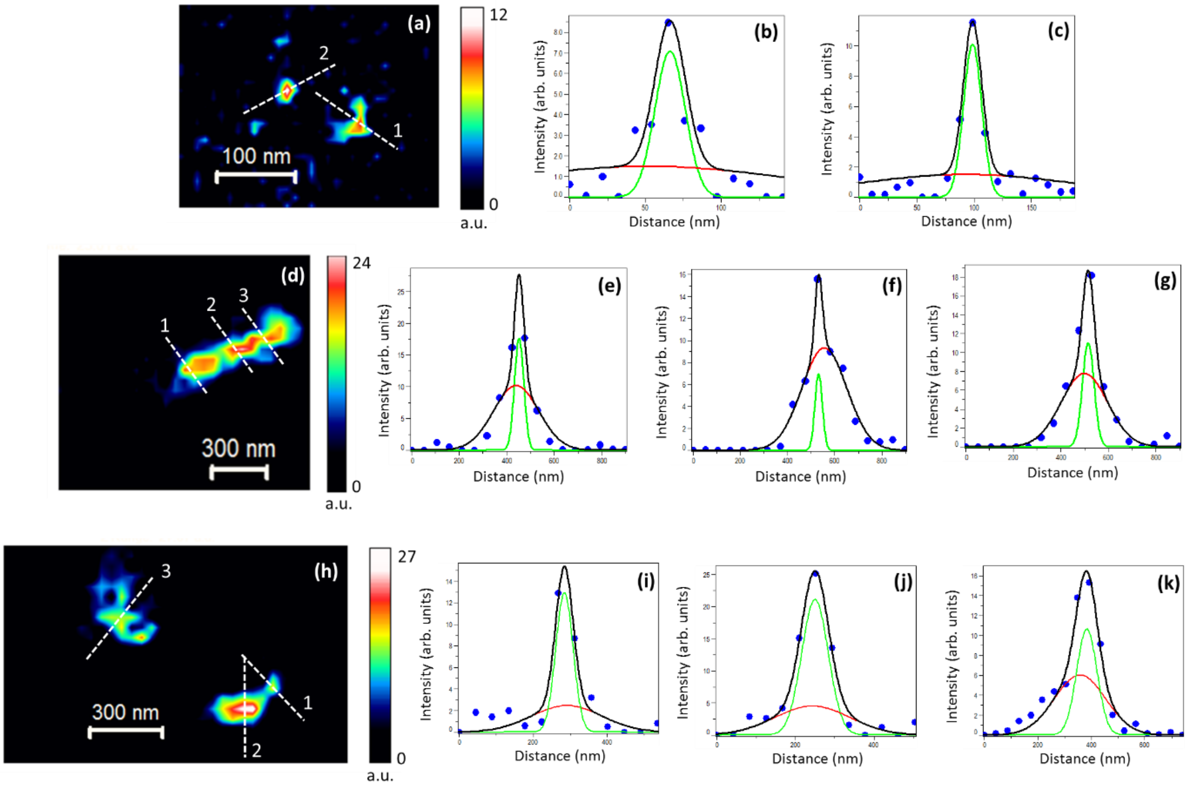

Fig. S10. Additional TERS maps of SWCNTs measured in water. (a) TERS map of the G-band intensity of a broken SWCNT measured in water on a glass substrate. Pixel size: 10 nm. (b) – (c) Plots of line profiles marked as 1-2 in (a) with fitted Gaussian curves for the far-field and near-field. The spatial resolution of the TERS map is estimated from the FWHM of the fitted Gaussian curves to be 22 ± 4 nm. We also measured TERS maps of SWCNTs with larger pixel sizes. (d) TERS map of the G-band intensity of a SWCNT measured in water on a glass substrate. Pixel size: 50 nm. (e) – (g) Plots of line profiles marked as 1-3 in (d) with fitted Gaussian curves for the far-field and near-field. The spatial resolution of the TERS map is estimated from the FWHM of the fitted Gaussian curves to be 47 ± 11 nm. (h) TERS map of the G-band intensity of a SWCNT measured in water on a glass substrate. Pixel size: 40 nm. (i) – (k) Plots of line profiles marked as 1-3 in (h) with fitted Gaussian curves for the far-field and near-field. The spatial resolution of the TERS map is estimated from the FWHM of the fitted Gaussian curves to be 62 ± 16 nm. The estimated spatial resolution of the TERS map in (d) should be treated with caution since the near-field signal of the SWCNT typically appears in only a few pixels along the line profiles and the pixel size is larger than the size of the near-field at the TERS tip-apex. Attempts at mapping the SWCNTs in (d) and (h) with a smaller pixel size were unsuccessful due to issues with SWCNT displacement during TERS imaging.

Table S1. Summary of the spatial resolution of SWCNT TERS images measured in air and water.

	TERS map	Pixel size of TERS map	Pixel size along the line profile (nm)	Spatial resolution (nm)	Mean spatial resolution (nm)
Air	Fig. S8a	10	10	26	28 ± 2
			10	29	
			10	28	
	Fig. S9a	10	10	19	22 ± 5
			10	28	
			10	20	
	Fig. S9e	17	17.0	27	27 ± 4
			17.5	31	
			17.7	23	
Water	Fig. S8e	10	10	28	26 ± 2
			10	25	
			10	26	
	Fig. S10a	10	10.4	24	22 ± 4
			10.7	19	
	Fig. S10d	50	53.5	46	47 ± 11
			54.0	37	
			52.3	58	
	Fig. S10h	40	42.3	55	62 ± 16
			41.7	80	
			42.7	51	

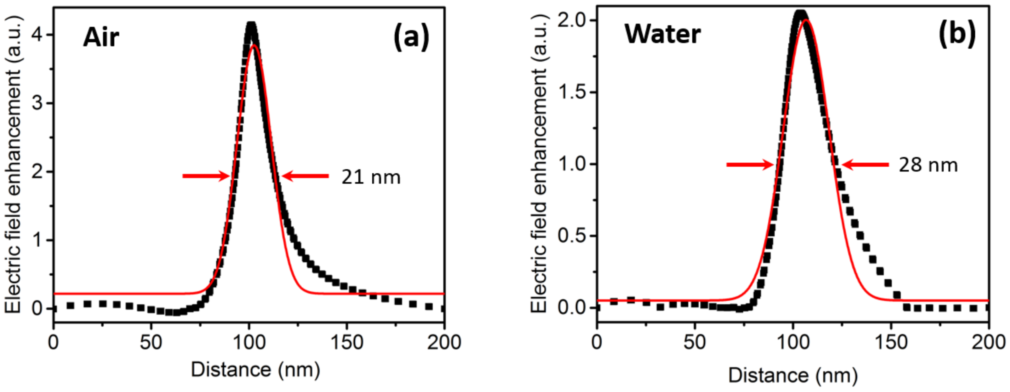

Fig. S11. Calculated horizontal intensity profiles beneath the tip-apex from the non-gap mode numerical simulations maps in (a) Fig. 4a (air) and (b) 4b (water) along with fitted Gaussian curves. Lateral size of near-field enhancement at the tip-apex in air and water is estimated from the FWHM of the fitted Gaussian curves to be 21 and 28 nm, respectively. The similar lateral size of the electric field enhancement in air and water indicates that a similar nanoscale spatial resolution is achievable for TERS imaging in air and water environments.